Structural rearrangement of the intracellular domains during AMPA receptor activation

Linda G. Zachariassen[a,1], Ljudmila Katchan[b,c,1], Anna G. Jensen[a], Darryl S. Pickering[a], Andrew J. R. Plested[b,c,2], and Anders S. Kristensen[a,2]

[a]Department of Drug Design & Pharmacology, University of Copenhagen, DK-2100 Copenhagen, Denmark; [b]Molecular Neuroscience and Biophysics, Leibniz-Institut für Molekulare Pharmakologie, 13125 Berlin, Germany; and [c]Cluster of Excellence NeuroCure, Charité Universitätsmedizin, 10117 Berlin, Germany

α-Amino-3-hydroxy-5-methyl-4-isoxazolepropionic acid receptors (AMPARs) are ligand-gated ion channels that mediate the majority of fast excitatory neurotransmission in the central nervous system. Despite recent advances in structural studies of AMPARs, information about the specific conformational changes that underlie receptor function is lacking. Here, we used single and dual insertion of GFP variants at various positions in AMPAR subunits to enable measurements of conformational changes using fluorescence resonance energy transfer (FRET) in live cells. We produced dual CFP/YFP-tagged GluA2 subunit constructs that had normal activity and displayed intrareceptor FRET. We used fluorescence lifetime imaging microscopy (FLIM) in live HEK293 cells to determine distinct steady-state FRET efficiencies in the presence of different ligands, suggesting a dynamic picture of the resting state. Patch-clamp fluorometry of the double- and single-insert constructs showed that both the intracellular C-terminal domain (CTD) and the loop region between the M1 and M2 helices move during activation and the CTD is detached from the membrane. Our time-resolved measurements revealed unexpectedly complex fluorescence changes within these intracellular domains, providing clues as to how posttranslational modifications and receptor function interact.

AMPA | glutamate | FRET | electrophysiology

The α-amino-3-hydroxy-5-methyl-4-isoxazolepropionic acid (AMPA)-type ionotropic glutamate receptors (iGluRs) reside in postsynaptic membranes in the central nervous system (1). Like the other major iGluR subtypes, the N-methyl-D-aspartate receptors (NMDARs) and kainate receptors, AMPARs are ligand-gated cation channels formed by hetero- or homotetrameric assembly of the GluA1 to GluA4 subunits into a membrane-spanning receptor with an integral ion channel. The energy from binding of the excitatory neurotransmitter glutamate at extracellular sites triggers AMPARs to passage through functional states that can include ion channel activation, deactivation, and desensitization. The timing and interplay between the necessarily distinct conformations of these states determine both basal transmission and short-term plasticity of the postsynapse (2–4).

Structures of AMPARs captured in various functional states using X-ray crystallography and cryoelectron microscopy have recently become available (5–9). Overall, the structures confirm three distinct structural layers (Fig. 1). The amino-terminal domain (ATD) and the ligand-binding domain (LBD), both distal to the membrane, and the transmembrane ion channel are each formed from four copies of the respective domain from each subunit. However, a fourth region of the receptor extends from the intracellular side of the membrane. This part of the receptor includes intracellular loops between the transmembrane helices and the variable C-terminal domain (CTD), and remains entirely unresolved in the presently available AMPAR structures.

The GluA2 structures and previous results from biochemical, biophysical, and crystallographic studies of isolated subunits and full-length receptors (2, 10–15) have provided a working model for understanding how agonist binding to the four clamshell-shaped LBDs pulls the linkers that connect the LBDs to the

pore-lining M3 helices away from the overall axis of the channel, and how desensitization can permit agonist-bound channels to be closed. However, if the intracellular domains play any structural role in activation and desensitization is unknown. Numerous studies have linked posttranslational modifications of the CTD with changes in receptor function, including gating (16, 17). To understand how these modifications can interact with the ion channel, it is essential to measure if and how the intracellular domains can undergo conformational changes.

Fluorescence resonance energy transfer (FRET) between two fluorophores can measure molecular distances and conformational changes within macromolecules such as proteins, including ion channels (18, 19). Previous studies have used fluorescence techniques in truncated iGluRs or their isolated domains to explore mechanisms of receptor activation (20–22), but concurrent measurements of function are lacking. In the present study, we engineered fluorescent GluA2 homotetrameric receptors and measured conformational changes within the receptor and in relation to the plasma membrane. We were able to track state-dependent conformational arrangements of the previously unresolved CTD and intracellular loops in the context of a full-length receptor to provide insight into the structural changes of this region during receptor function.

Significance

α-Amino-3-hydroxy-5-methyl-4-isoxazolepropionic acid receptors (AMPARs) are the main excitatory receptors in the brain. Although neurotransmitter binding to AMPARs is well understood, knowledge regarding their activation mechanisms remains incomplete. We exploited genetic insertion of fluorescent proteins to create AMPARs displaying fluorescence resonance energy transfer and allow optical monitoring of conformational changes in the receptor. Ligand-driven conformational changes are observed to occur in two intracellular domains of the receptor that are distant from the extracellular site where glutamate binds. The C terminus extends laterally from the receptor and remains relatively close to the plasma membrane. By measuring the activation of receptors electrically and optically at the same time, this study reveals AMPAR conformational changes occurring during receptor state transitions for a region not resolved in structural studies.
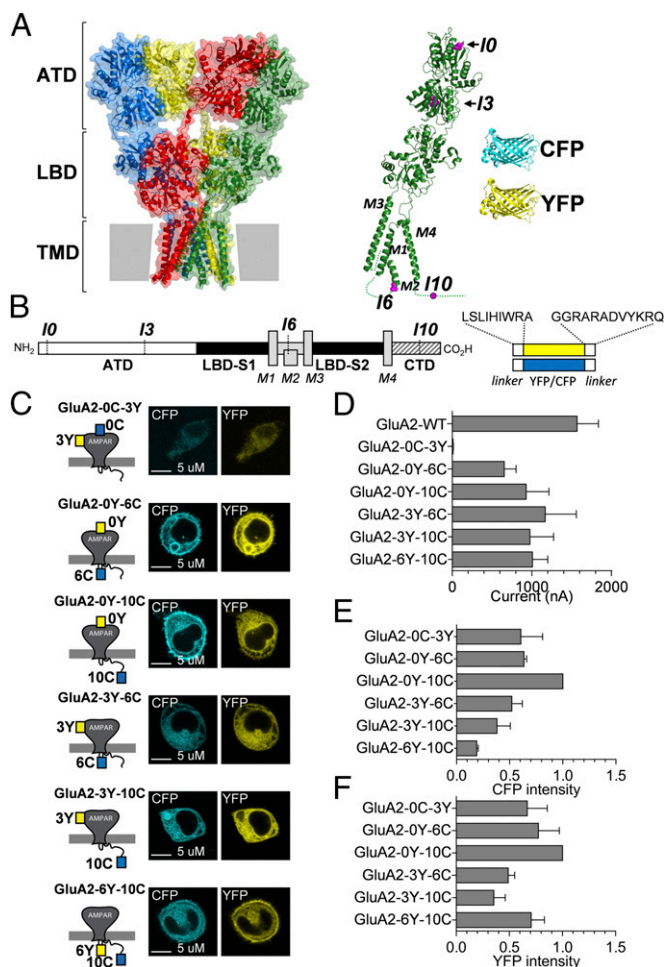

Fig. 1. Design and characterization of GluA2-CFP/YFP fusion constructs. (*A*) Surface representation of the X-ray crystal structure of the GluA2 receptor (Protein Data Bank ID code 3KG2) (6) with domains (ATD, LBD, and TMD) indicated. Each of the four subunits is highlighted in a different color. To the *Right* is shown a ribbon representation of the structure of a single GluA2 subunit (green) with the structures of CFP (blue) and YFP (yellow) shown to scale. The insertion sites I0, I3, I6, and I10 are highlighted in magenta. (*B*) Schematic overview of GluA2 subunit topology and FP insertions. (*C*) Confocal micrographs of CFP (*Left*) and YFP (*Right*) fluorescence in HEK293 cells transfected with the GluA2-CFP/YFP fusion constructs. (*D*) Summary of amplitudes of membrane currents evoked by glutamate (0.1 mM) in *Xenopus* oocytes expressing GluA2-CFP/YFP constructs held at a membrane potential of −60 mV (*Materials and Methods*). Data represent mean ± SEM for six to 12 oocytes. A summary of relative emission intensities for CFP (*E*) and YFP (*F*) in suspensions of transfected HEK cells transfected with GluA2-CFP/YFP constructs is provided. Data are shown normalized to the intensity measured for GluA2-0Y-10C and represent the mean ± SEM of three independent transfection experiments.

Results

GluA2 Subunits with Internal Insertion of YFP. Guided by previous work (23), we inserted a cDNA fragment encoding a yellow variant of GFP, Venus (which we refer to here as YFP; *Materials and Methods*), flanked by short flexible linkers in various positions into a synthetic rat GluA2 coding sequence (GluA2m) to generate 11 unique GluA2-YFP fusion constructs (termed GluA2-0Y to GluA2-10Y) (Fig. S1 and Table S1). Inspection of confocal micrographs showed seven of these GluA2-YFP constructs expressed in HEK293T cells (GluA2-0Y, GluA2-1Y, GluA2-2Y, GluA2-3Y, GluA2-6Y, GluA2-7Y, and GluA2-10Y) to display bright, membrane-localized fluorescence. The remaining constructs showed either weak or no fluorescence. Bulk fluorescence

measurements of cell suspensions corroborated the impression from the confocal images (Fig. S1 *B and C*). Two-electrode voltage-clamp electrophysiology (TEVC) characterization of the ability of the 11 constructs to form functional receptors revealed that all of the constructs with bright fluorescence except GluA2-2Y displayed robust responses to glutamate with EC_{50} values and maximum current amplitudes similar to those responses obtained from the parent GluA2m and WT GluA2, whereas the remaining constructs produced no detectable current (Fig. S1*B* and Table S1). Together, these results confirm and extend previous studies (23, 24) showing that positions in the extreme N terminus (I0), the ATD (I1, I2, and I3), the M1/M2 loop (I6 and I7), and the CTD (I10) are permissive for insertion of fluorescent protein (FP) variants with surprisingly limited effects on receptor activity and expression. To enable measurements of potential intramolecular FRET within the subunits of homomeric GluA2 receptors, we next inserted a cyan variant of GFP, mCerulean3 (25) (which we refer to here as CFP; *Materials and Methods*) at the permissive positions I0, I3, I6, or I10 in the GluA2-YFP constructs. We hereby created a total of six unique dual-tagged GluA2-CFP/YFP constructs, representing all possible combinations of dual-FP insertions in the I0, I3, I6, and I10 positions (Fig. 1). Confocal images and analysis of emission scans of HEK293T cells transfected individually with the six constructs showed that all constructs produced fluorescence emission in spectral bands unique for CFP and YFP (Fig. 1 *C, E,* and *F*). TEVC characterization of the function of the constructs expressed in oocytes showed that inward currents evoked by glutamate application had similar magnitudes to the parent GluA2m construct, except for the GluA2-0C-3Y construct, which was apparently nonfunctional, perhaps reflecting steric clashes between these two sites that prevented proper subunit assembly or membrane trafficking (Fig. 1*D*). The positive allosteric modulator cyclothiazide (CTZ) and the competitive antagonist 6,7-dinitroquinoxaline-2,3-dione (DNQX) were characterized independently at the functional GluA2-CFP/YFP constructs expressed in oocytes, along with determination of glutamate EC_{50} (Fig. S2 and Table S2). Overall, the pharmacological properties of the constructs were similar to WT GluA2 (Fig. S2 and Table S2), except for GluA2-3Y-6C and GluA2-6Y-10C, which displayed approximately fivefold decreased IC_{50} values for DNQX compared with WT GluA2. The increased potency of DNQX, in the absence of any change in apparent glutamate affinity, suggested that LBD binding site mobility might be unexpectedly sensitive to distant fluorescent insertions, which we explore below.

Determination of FRET in GluA2-CFP/YFP Receptors. For initial characterization of potential FRET, we analyzed fluorescence emission from HEK293T cells transfected with the individual constructs using excitation at 430 nm, which is close to the absorption maximum of CFP but essentially outside the absorption range of YFP (Fig. 2*A*). To produce control constructs, we introduced the Y67C mutation into YFP, thus creating the variant denoted amber that folds correctly but does not form a chromophore, and thus cannot act as a FRET acceptor (26) (*Materials and Methods*). The emission spectra for GluA2-0Y-10C, GluA2-3Y-6C, and GluA2-3Y-10C and the corresponding amber constructs (GluA2-0A-10C, GluA2-3A-6C, and GluA2-3A-10C) were indistinguishable, strongly suggesting that there is no FRET between CFP and YFP at these positions (Fig. 2*A*). In contrast, cells transfected with GluA2-6Y-10C displayed an approximately threefold increase in relative emission at 530 nm compared with the non-FRET control GluA2-6A-10C, which was indistinguishable from the other amber constructs or CFP expressed alone (Fig. 2*A*).

To determine the FRET efficiency for GluA2-6Y-10C, we used fluorescence lifetime imaging microscopy (FLIM) (Fig. 2 *B–D*). Using time-correlated, single-photon counting (*Materials and Methods*), we determined the fluorescence lifetime of CFP (τ_{CFP}) in cells expressing each of the five functional GluA2-CFP/YFP constructs and in cells expressing the corresponding GluA2-CFP/amber control constructs (Table 1). The τ_{CFP} should be

reduced if FRET occurs in the GluA2-CFP/YFP receptors, compared with the τ_{CFP} in cells expressing the equivalent amber receptors. Fig. 2B shows recorded lifetime maps for two representative cells, expressing GluA2-6Y-10C and GluA2-6A-10C receptors, respectively. The results showed that τ_{CFP} was unchanged between cells expressing GluA2-0Y-6C, GluA2-0Y-10C, GluA2-3Y-6C, and GluA2-3Y-10C and the equivalent amber constructs (3.38–3.46 ns; Table 1). Thus, echoing the impression from emission spectra, there was no FRET between fluorophores placed N-terminal to the ATD (insertion site I0) or in the ATD/LBD linker (insertion site I3) and fluorophores inserted in the intracellular domains (insertion sites I6 and I10, respectively). This observation was perhaps unsurprising, considering that the Förster distance (R_0) is ~50 Å for the CFP-YFP pair (27, 28) and the efficiency of FRET between these fluorophores thus approaches 0 at ~100 Å, due to the sixth-power dependence (Materials and Methods). According to available GluA2 structures (6), the distance between these two regions is ~120–170 Å. These insertions thus served as internal controls for the specificity of FRET between distinct insertion sites.

In contrast, for cells expressing the GluA2-6Y-10C construct, the τ_{CFP} was robustly decreased (to 3.05 ± 0.02 ns), compared with the average τ_{CFP} observed in cells expressing the FRET knockout amber construct GluA2-6A-10C (from 3.52 ± 0.03 ns; Table 1). This reduction corresponded to a FRET efficiency of 13.4% (Materials and Methods and Table 1). Swapping the positions of the CFP and YFP within the dual insertion (GluA2-6C-10Y) gave an indistinguishable reduction in donor lifetime (Table 1). These results reinforce the finding that FRET occurs between fluorophores in the intracellular loop between M1 and M2 and fluorophores positioned in the intracellular CTD (Fig. 1).

Kinetic Characterization of Receptors with Single- and Double-Fluorescent Insertions. During synaptic transmission, AMPARs are activated with rapid kinetics by glutamate transients of about 1 ms in duration (29). To confirm that the fluorescently tagged GluA2 constructs were a good surrogate for AMPARs with normal fast gating, we compared the deactivation, desensitization, and recovery from desensitization of GluA2-6Y-10C, GluA2-6Y, and GluA2-10Y receptors to WT GluA2 receptors expressed in HEK cells using fast perfusion patch-clamp electrophysiology. In outside-out patches, both dual-fusion (GluA2-6Y-10C) and single-fusion (GluA2-6Y and GluA2-10Y) receptors had similar kinetic properties to WT GluA2 (Fig. S3). The desensitization rates (k_{des}) of the fusion receptors during a long (100 ms) pulse of 10 mM glutamate ($k_{des\ 6Y-10C} = 168 \pm 31\ s^{-1}$, $k_{des\ 6Y} = 143 \pm 18\ s^{-1}$, and $k_{des\ 10Y} = 168 \pm 13\ s^{-1}$) were close to WT GluA2 desensitization rates ($k_{des\ WT} = 135 \pm 26\ s^{-1}$; Fig. S3 A and B). For GluA2-6Y-10C, the rates of deactivation (k_{deact}) in response to a short (1 ms) pulse of glutamate ($k_{deact\ 6Y-10C} = 2,300 \pm 230\ s^{-1}$, $k_{deact\ 6Y} = 1,370 \pm 150\ s^{-1}$, and $k_{deact\ 10Y} = 1,700 \pm 150\ s^{-1}$) were likewise similar to WT ($k_{deact\ WT} = 1,990 \pm 150\ s^{-1}$; Fig. S3 D and E). On the other hand, GluA2-6Y-10C recovered from desensitization slightly slower ($k_{rec\ 6Y-10C} = 34 \pm 5\ s^{-1}$; Fig. S3C) than WT ($k_{rec} = 57 \pm 6\ s^{-1}$), where k_{rec} is the rate of recovery, whereas single fusions were essentially unaffected ($k_{rec\ 6Y} = 48 \pm 8\ s^{-1}$ and $k_{rec\ 10Y} = 50 \pm 5\ s^{-1}$). In summary, these data show that GluA2 receptors with one or two inserted fluorophores at the I6 and I10 positions have a functional phenotype very similar to WT GluA2 receptors, maintaining fast activation and desensitization with, in one case, a slightly slowed recovery from desensitization.

Ligand Binding Induces Changes in FRET Between YFP in M1-M2 Loop Region and CFP in CTD. We reasoned that because FRET efficiency steeply depends on distance between fluorophores, the magnitude of the FRET signal between the two FP insertions could report state-dependent movement in iGluRs. We first performed FLIM measurements of the fluorescence lifetime of CFP localized in the surface membrane of cells expressing GluA2-6Y-10C or GluA2-6A-10C constructs at equilibrium following
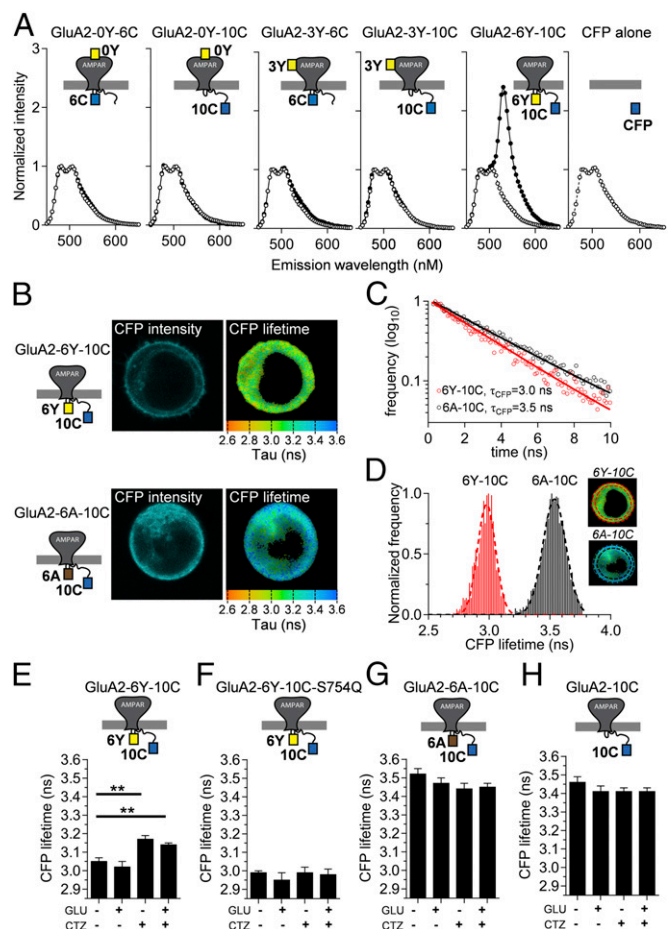

Fig. 2. Evaluation of FRET in GluA2-CFP/YFP receptors. (A) FRET spectra of suspensions of HEK cells transfected with GluA2-CFP/YFP constructs (●) and their GluA2-CFP/amber (○) equivalents are shown. Spectra show normalized emission relative to the peak of the CFP emission at 480 nm obtained using CFP excitation (430 nm). An emission spectrum for cells expressing CFP (○) alone is shown for comparison. A, amber; C, CFP; Y, YFP. (B) Confocal images of CFP emission (CFP intensity) and fluorescence lifetime (CFP lifetime) in HEK293 cells expressing the GluA2-6Y-10C construct or the FRET-deficient amber equivalent GluA2-6A-10C were obtained by confocal microscopy as described in Materials and Methods. Donor fluorescence lifetimes (τ_{CFP}) were acquired at each pixel by fitting the time course of fluorescence decay obtained by TCSPC analysis (Materials and Methods), and used to construct fluorescence lifetime images where pixel color corresponds to the measured CFP lifetime as indicated by scale bars. (C) Determination of τ_{CFP} in the presence and absence of acceptor YFP in a single representative pixel in the lifetime images of the GluA2-6Y-10C– or GluA2-6A-10C–expressing cells shown in B. Decay of GluA2-6A-10C (black circles) represents the donor fluorescence lifetime in the absence of acceptor, whereas GluA2-6Y-10C (red circles) represents the donor lifetime in the presence of YFP. Both decays follow a single exponential time course. (D) Frequency distribution histograms of lifetime values from individual pixels in the FLIM images (Right Insets) within the surface membrane region (demarcated with red and black punctuated lines) of the cells expressing GluA2-6Y-10C (Upper Inset) and GluA2-6A-10C (Lower Inset). The lifetime distributions for CFP in the representative cells expressing GluA2-6Y-10C (red) and GluA2-6A-10C (black) were fitted to a single binomial (Materials and Methods) to determine the mean ± SD of the lifetime values of CFP in the absence (3.54 ± 0.09 ns) and presence (2.98 ± 0.07 ns) of acceptor, respectively. Summaries of CFP lifetimes obtained from cells expressing GluA2-6Y-10C (E), the CTZ-insensitive mutant GluA2-6Y-10C-S754Q (F), the amber equivalent GluA2-6A-10C (G), and the donor-alone GluA2-10C (H) obtained under different ligand conditions are shown. **$P < 0.01$, compared with no ligand condition.

incubation with glutamatergic ligands (Materials and Methods and Table 2). In the absence of ligand, receptors on the surface of the cells should mainly reside in the resting conformation, whereas in

Table 1. CFP fluorescent lifetimes and CFP/YFP Förster efficiency in dual-tagged GluA2-CFP/YFP receptors

Receptor	FP donor	FP acceptor	τ_{CFP},[†] ns	n	E,[‡] %
GluA2-0Y-6C	CFP	YFP	3.45 ± 0.02	11	0
GluA2-0A-6C	CFP	amber	3.44 ± 0.01	10	—
GluA2-0Y-10C	CFP	YFP	3.43 ± 0.05	8	0
GluA2-0A-10C	CFP	amber	3.46 ± 0.04	10	—
GluA2-3Y-6C	CFP	YFP	3.38 ± 0.03	11	0
GluA2-3A-6C	CFP	amber	3.45 ± 0.01	8	—
GluA2-3Y-10C	CFP	YFP	3.43 ± 0.03	14	0
GluA2-3A-10C	CFP	amber	3.42 ± 0.03	7	—
GluA2-6Y-10C	CFP	YFP	3.05 ± 0.02*	14	13.4
GluA2-6A-10C	CFP	amber	3.52 ± 0.03	10	—
GluA2-6C-10Y	CFP	YFP	3.10 ± 0.03	8	10.6
GluA2-6C	CFP	—	3.46 ± 0.03	8	

E, FRET efficiency; ns, nanoseconds.

*$P < 0.05$ compared with the corresponding amber-containing receptor.

[†]Fluorescence lifetime for CFP was obtained by FLIM analysis as described in *Materials and Methods* in the presence of YFP or the FRET-incapable YFP variant amber. Data represent the mean ± SEM of the average lifetime observed in n different cells.

[‡]FRET efficiency for intrareceptor FRET in GluA2-CFP/YFP receptors was calculated from the values of τ_{CFP} obtained in presence and absence of YFP as described in *Materials and Methods*.

the continued presence of glutamate, the vast majority of receptors should reside in the desensitized state. The mean τ_{CFP} obtained in the presence of glutamate was identical to the τ_{CFP} obtained in the absence of agonist (3.02 ± 0.03 ns with glutamate vs. 3.05 ± 0.02 ns in its absence; $P > 0.05$; Fig. 2E). To access the active state, we included CTZ, which binds within the interface of the LBDs and inhibits transition into the desensitized state (11). The τ_{CFP} obtained from the GluA2-6Y-10C in the presence of CTZ and glutamate was greater than the τ_{CFP} in the absence of added ligand (3.14 ± 0.01 ns with glutamate and CTZ; $P < 0.05$ vs. no ligand or vs. glutamate alone). CTZ alone also yielded a τ_{CFP} that was significantly increased (3.17 ± 0.02 ns; $P < 0.05$) compared with the τ_{CFP} in the absence of ligand, as well as the τ_{CFP} in the presence of glutamate alone (Fig. 2E). FLIM measurements from the corresponding amber construct GluA2-6A-10C (Fig. 2G) or donor-alone construct GluA2-10C (Fig. 2H) showed τ_{CFP} in the absence of acceptor to be independent of the glutamatergic ligands applied. Calculation of FRET efficiencies from the values of τ_{CFP} in the absence and presence of YFP obtained in either condition shows that the observed differences in τ_{CFP} between cells in the presence and absence of CTZ correspond to a change in FRET efficiency from 13.4% in the absence of CTZ to 8.0% (CTZ alone) and 9.0% (CTZ and Glu) (Table 2). Critically, a mutation in the binding site for CTZ that eliminates its action, S754Q (30), blocked the increase in τ_{CFP} produced by CTZ (Fig. 2F), indicating that CTZ binding to the extracellular site is responsible for the lifetime change, and ruling out any spurious additional binding sites or nonspecific effects (Table 2). These results show that CTZ binding to GluA2-6Y-10C induced a shift in the conformational equilibrium of the receptor population, during both the resting and activated state conditions.

The distinct changes in donor lifetime emboldened us to measure changes in FRET during receptor activation using patch-clamp fluorometry. We used a ratiometric spectral FRET approach (31) to detect fluorescence changes from GluA2-6Y-10C expressed in HEK293 cells simultaneously with recording of GluA2-6Y-10C currents. We applied glutamate in the presence and absence of CTZ to compare the responses of the receptor in its resting, active, and desensitized states. Consistent with FLIM measurements at equilibrium, there was a detectable decrease in FRET efficiency (from emission spectral ratios) during constant CTZ application compared with FRET efficiency in the absence of CTZ (Fig. 3C). In contrast, glutamate binding and receptor

activation did not cause a detectable change in FRET. To measure the effect of CTZ binding on FRET between the intracellular loops and CTD in GluA2-6Y-10C, we collected spectra generated from alternating donor and acceptor excitation during the first exposure of a naïve cell to a single prolonged application of CTZ and glutamate, and compared them with an equally long application of glutamate in absence of CTZ (Fig. 3D). Slow CTZ binding could be monitored from the gradual relief of desensitization, which occurred with a time constant of 1.5 ± 0.1 s, and began to develop during the first 50 ms of the CTZ application. During CTZ exposure, the FRET efficiency decreased compared with baseline before the application of CTZ by 4% ($P = $ 8E-05; Fig. 3D). FRET efficiency did not immediately return to baseline levels after glutamate unbinding, consistent with slow release of CTZ from receptors, further suggesting that bound CTZ affects the arrangement of the intracellular domains in the absence of ligand. The discrepancy between the apparent FRET changes during steady state and acute application of CTZ is likely due to a difference in the time of exposure to CTZ. At steady-state conditions, exposure to CTZ lasts for several minutes before the onset of the recording, whereas during acute application of CTZ, the exposure time is limited to ≈25 s.

To ensure the specificity of the effect of CTZ, we again exploited the S754Q mutation, which blocked any functional effect of CTZ on currents as expected (11) (Fig. 3 C and D). Echoing the fluorescence lifetime measurements, the effect of CTZ on FRET efficiency was lost in the S754Q mutant of GluA2-6Y-10C during both constant and acute application of CTZ (Fig. 3 C and D, Lower). Application of the inactive D-isomer of glutamate to either the double-insertion construct or the S754Q mutant failed to provoke a detectable FRET signal with the same protocol (Fig. S4). The lifetime measurements, together with the spectral FRET data, suggest that extracellular binding

Table 2. CFP fluorescent lifetimes and CFP/YFP Förster efficiency in dual-tagged GluA2-6Y-10C receptors in the presence of glutamate and CTZ

Receptor	I6 insert	I10 insert	Ligand	τ_{CFP},[†] ns	n	E,[‡] %
GluA2	CFP	YFP	None	3.05 ± 0.02	31	13.4
GluA2	CFP	amber	None	3.52 ± 0.03	17	—
GluA2	CFP	—	None	3.46 ± 0.03	8	—
GluA2-S754Q	CFP	YFP	None	2.99 ± 0.01	11	16.8
GluA2-S754Q	CFP	amber	None	3.56 ± 0.01	11	—
GluA2	CFP	YFP	GLU	3.02 ± 0.03	15	12.7
GluA2	CFP	amber	GLU	3.47 ± 0.03	11	—
GluA2	CFP	—	GLU	3.41 ± 0.03	8	—
GluA2-S754Q	CFP	YFP	GLU	2.95 ± 0.04	10	18.2
GluA2-S754Q	CFP	amber	GLU	3.60 + 0.01	10	—
GluA2	CFP	YFP	CTZ	3.17 + 0.02*	9	8.0
GluA2	CFP	amber	CTZ	3.44 ± 0.03	9	—
GluA2	CFP	—	CTZ	3.41 + 0.02	6	—
GluA2-S754Q	CFP	YFP	CTZ	2.99 + 0.03	11	16.8
GluA2-S754Q	CFP	amber	CTZ	3.59 + 0.01	10	—
GluA2	CFP	YFP	GLU + CTZ	3.14 ± 0.01*	10	9.0
GluA2	CFP	amber	GLU + CTZ	3.45 ± 0.02	10	—
GluA2	CFP	—	GLU + CTZ	3.40 ± 0.02	8	—
GluA2-S754Q	CFP	YFP	GLU + CTZ	2.98 ± 0.03	13	17.9
GluA2-S754Q	CFP	amber	GLU + CTZ	3.63 ± 0.03	10	—

GLU, glutamate.

*$P < 0.05$ compared with same construct with no ligand.

[†]Fluorescence lifetime for CFP in the presence of GLU (1,000 μM) and/or CTZ (25 μM) was obtained by FLIM analysis as described in *Materials and Methods*. Data represent the mean ± SEM of the average lifetime observed in n different cells.

[‡]FRET efficiency was calculated as described in *Materials and Methods* from CFP lifetimes obtained for GluA2-6Y-10C and the corresponding donor-only amber construct.

of CTZ produces a specific arrangement of the intracellular domains of the receptor.

Voltage-Dependent Quenching of YFP in the Intracellular Regions by a Membrane-Bound Quencher. Although the approximate position of the I6 insertion (i.e., within the turret domain formed by the M1-M2 intracellular loop regions, near to the pore axis) can be inferred from the GluA2 structures, the I10 insertion cannot. This position is located in the CTD, which is truncated by 36 residues in all of the existing GluA2 constructs that have been successfully crystallized to date. Thus, the spatial orientation of the CTD relative to the transmembrane domain (TMD) is essentially unknown. To determine the arrangement of the I6 and I10 insertion sites better and to assess their potential orthogonal movements relative to the plasma membrane, we measured quenching of single YFP insertions by a nonfluorescent membrane-bound anionic quencher, dipicrylamine (DPA). We initially characterized fluorescence from cells expressing GluA2 with YFP insertions at the I6 (GluA2-6Y) or I10 (GluA2-10Y) position by measuring YFP emission spectra during prolonged (5 s) applications of glutamate in the absence and presence of CTZ with constant perfusion of DPA (5 µM). The spectra were collected from whole cells clamped at −40 mV. In this condition, the DPA molecules reside mainly in the outer leaflet of the plasma membrane (Fig. 4A). Strikingly, we found that YFP showed similar state-dependent relative changes in fluorescence at both insertion sites (Fig. 4B). The mean increases in YFP intensity were 11% and 7% for GluA2-6Y and GluA2-10Y, respectively, in the desensitized state (Fig. 4B). The intensity of YFP at the I6 and I10 sites decreased by 10% and 6%, respectively, when receptors were activated by glutamate in the presence of CTZ (Fig. 4B). The onset and recovery of the fluorescence signals generated by long applications were considerably slower than receptor-gating kinetics, with the following time constants: $\tau_{\text{on\_des 6Y}} = 1.3 \pm 0.2$ s, $\tau_{\text{off\_des 6Y}} = 0.9 \pm 0.03$ s ($n = 11$) and $\tau_{\text{on\_des 10Y}} = 1.1 \pm 0.4$ s, $\tau_{\text{off\_des 10Y}} = 1.2 \pm 0.1$ s ($n = 8$) for the desensitized state of GluA2-6Y and GluA2-10Y, and $\tau_{\text{on\_act 6Y}} = 1 \pm 0.1$ s, $\tau_{\text{off\_act 6Y}} =$ 3 ± 1 s ($n = 9$) and $\tau_{\text{on\_act 10Y}} = 0.7 \pm 0.1$ s, $\tau_{\text{off\_act 10Y}} = 1.6 \pm 0.1$ s ($n = 6$) for the active state.

We subsequently chose the I6 insertion site, for its higher relative change in fluorescence and the position adjacent between transmembrane helices, to investigate whether faster acquisition rates (100 Hz) (Fig. 4C) could resolve fluorescence signals with similar kinetics to receptor gating during activation and desensitization. Fast (100 ms) applications of glutamate to cells expressing GluA2-6Y showed that the extent and rate of activation were concentration-dependent in the presence of CTZ, both for fluorescence and current (Fig. 4 C and D). Application of subsaturating glutamate (100 µM) evoked quenching of fluorescence in the active state that developed with time constant $\tau_{\text{F, act}} = 13$ ms, corresponding to the current activated with time constant $\tau_{\text{act}} = 8.5$ ms (Fig. 4D, black vs. purple squares). Under application of saturating concentrations of glutamate, the fluorescence signal developed with $\tau_{\text{F, act}} = 10$ ms, whereas the time constant for current onset was $\tau_{\text{act}} = 3.5$ ms (Fig. 4D, black vs. green triangles). Under desensitizing conditions in the absence of CTZ, fluorescence emission increased with $\tau_{\text{F,des}} = 29$ ms, whereas the rate of desensitization was $\tau_{\text{des}} = 9.4$ ms (Fig. 4D, black vs. red circles). The slower onset of the fluorescence signal under desensitizing conditions might be explained by superposition of the fluorescence signal from the channel opening on the desensitized signal. These measurements show that the fluorescence signals from GluA2-6Y report receptor activation, and a conformation of the ion channel pore, distinct from the resting state, exist for the desensitized state.

The FRET efficiency between donor and acceptor in the I6 and I10 positions measured by FLIM implies an average separation of >60 Å between the inserted FPs. The I10 insertion could conceivably give similar FRET while occupying any position within a 90° arc, from a radially distant site adjacent to the membrane, to a point directly below the channel and adjacent to its axis (Fig. 5A). To determine the state-dependent arrangement of the intracellular domains containing the two insertion sites, we took advantage of the mobile nature of DPA, which can be

Fig. 3. Characterization of the GluA2-6Y-10C receptor FRET by voltage-clamp fluorometry. (A) Cartoon representation of a dual-tagged AMPAR with YFP inserted in the intracellular loop between M1 and M2 transmembrane helices and CFP inserted in the C-terminal tail. (B) Schematic representation of the protocol used for simultaneous acquisition of fluorescence spectra and current, and a representative train of collected spectra. (C) Averaged FRET traces, with the SD indicated by pale shading, and representative time-locked current traces from cells expressing GluA2-6Y-10C (6Y-10C; *Upper*, n = 8) and the corresponding S754Q mutant (6Y-10C-S754Q; *Lower*, n = 5). Traces were recorded in the presence and absence of CTZ (green and red traces, respectively). Ratiometric FRET was calculated as described in *Materials and Methods* from emission spectra obtained at 10 Hz. The data were normalized on a frame-by-frame basis to the control condition (absence of CTZ) to allow comparison of the equilibrium values. Averaged acceptor emission spectra following donor excitation at 445 nm are shown for both conditions from the point during the recording indicated by the box. (D) Average spectral FRET recording of GluA2-6Y-10C (*Upper*, n = 20) and GluA2-6Y-10C S754Q (*Lower*, n = 19) constructs in a total of 18 frames during a prolonged (20 s) exposure to glutamate (red traces) or glutamate and CTZ (green traces). Due to the limited speed of fluorescence recording for FRET experiments (0.5 Hz), the time course of CTZ-induced FRET decrease was not resolved. The data were normalized to the baseline before the jump. Boxes indicate samples compared between green and red traces with an unpaired two-tailed Student's t test (P = 8E-05 for the last sample during CTZ application). The averaged acceptor emission spectra for the boxed regions collected in the presence (green) and absence (red) of CTZ are shown for both the GluA2-6Y-10C and the S754Q mutant.
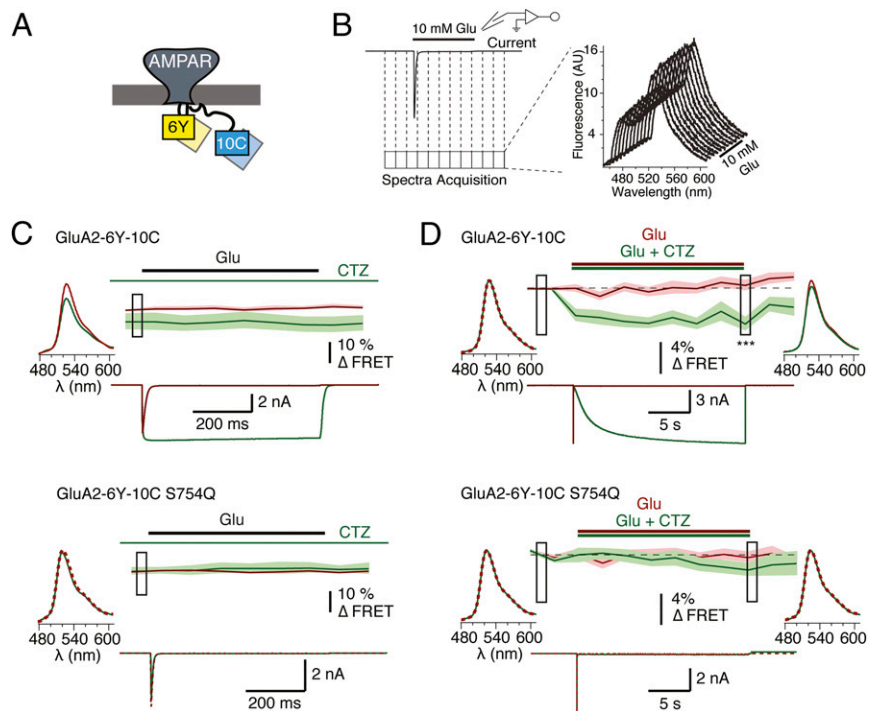
translocated ~25 Å between the inner and outer leaflets of the plasma membrane (32) with voltage (Fig. 5A). Hybrid voltage sensors exploit this property to report voltage changes with fluorescence intensity (33). Because the degree and the half-voltage of donor quenching are expected to depend on the axial distance of the donor from the membrane, and on FRET R_0, we reasoned that the voltage dependence of fluorescence would pinpoint the positions of the insertion sites relative to the membrane. To validate this principle, we first expressed GFP and YFP constructs with identical membrane-anchoring sequences (Materials and Methods). We recorded fluorescence intensity during 1-s voltage ramps (−120 to +120 mV; Fig. 5B) and removed apparent hysteresis due to voltage-dependent accumulation or depletion of DPA into the membrane by running the ramps in both directions and averaging intensities. Consistent with theoretical predictions, and previous work (33, 34), membrane-anchored GFP and YFP had different half-maximal quenching voltages (V_{Q50}: −47 ± 7 and −29 ± 4 mV; Fig. 5C and Fig. S5) and distinct extents of quenching (55% and 30%) despite indistinguishable plasma membrane expression. The distinct quenching profiles were likely due to the different R_0 distances between GFP or YFP and DPA molecules: 37 Å and 31 Å, respectively (33). Next, we collected similar spectra of YFP from DPA-treated cells expressing GluA2-6Y and GluA-10Y before and during long applications of glutamate (5 s) in the presence or absence of CTZ, thereby enabling us to determine the V_{Q50} for YFP in either position for each respective functional state (Fig. 5 B and D). The half-voltages of YFP in both I6

and I10 positions were similar to membrane-attached YFP (Fig. S5). Unfortunately, the shallowness of the quenching with voltage [due to the low fraction of the electric field traversed by DPA (0.6)] (35) did not allow us to determine the V_{Q50} precisely enough to assign distances to different states. However, the extents of quenching (Fig. 5 E and F) provided unequivocal information about the fluorophore positions.

Fig. S6 shows theoretical relationships between donor fluorescence intensity and YFP/DPA distance, at infinite negative and positive potentials, and the difference between them (ΔF). We used these curves to discern the axial distance of FPs from the membrane. In an infinitely depolarized membrane, DPA preferentially resides in the inner leaflet (Fig. 5A); thus, donor fluorescence reduces in a saturating manner before the FP is sterically hindered by its size from further approach. Infinite hyperpolarization moves DPA to the outer leaflet (25 Å further away from the donor). In this condition, quenching only develops at closer distances and cannot saturate. Therefore, the predicted voltage-dependent ΔF peaks around 25 Å from the membrane (Fig. S6). Because we do not know the absolute scale of fluorescence, or of the background, we scanned a range of values for each as a correction to the theoretical curves. In this way, we found a unique set of distances for each insert in the three states that could satisfy the expected voltage-dependent quenching (Materials and Methods and Fig. S6).

We obtained axial distances (between the I6 chromophore and DPA) of 12 Å for the active state, 20 Å for the resting state, and 35 Å for the desensitized state. Quenching of YFP in the I10
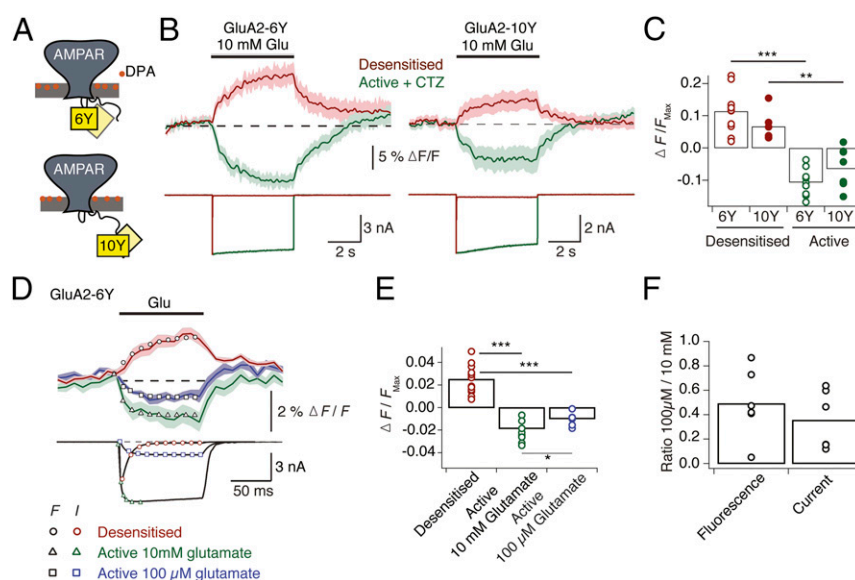

Fig. 4. Single-fusion quenching by DPA. (A) Cartoon representation of the orientation of the nonfluorescent quencher DPA relative to YFP in GluA2-6Y and GluA2-10Y at hyperpolarized membrane potential (35). (B, Upper) Averaged peak fluorescence emission of GluA2-6Y (Left) and GluA2-10Y (Right) recorded at 20 Hz from whole cells during long (5 s) exposures of glutamate (10 mM) in the presence (green; n = 9) and absence (red; n = 11) of CTZ (100 μM). Cells were clamped at −40 mV under constant DPA perfusion. Pale shading indicates the SD of the mean. (B, Lower) Representative simultaneous current recordings with the same color scheme. Calculation of $\Delta F/F$ is described in Materials and Methods. (C) Summary of maximal changes in the peak of the fluorescence spectrum (the average of the final three samples during the glutamate application) in response to a 5-s glutamate application in the absence (red) and presence (green) of CTZ. Changes in fluorescence in the absence of CTZ represent receptor transition from the resting state to the desensitized state, whereas the changes in fluorescence in the presence of CTZ represent the transition to the active state. Points indicate responses from individual cells, and the bars represent the mean. (D) Fluorescence emission and membrane current from cells expressing GluA2-6Y in the presence of DPA in response to a brief (100 ms) stimulus with a saturating concentration of glutamate (10 mM) (red, n = 13), saturating concentration of glutamate (10 mM) and CTZ (100 μM) (green, n = 10), and subsaturating concentration of glutamate (0.1 mM) (purple, n = 6). The fluorescence signal was recorded at 100 Hz. Average fluorescence changes and individual currents were independently fit with single exponentials, yielding the following time constants: desensitization (F, black circles, τ = 29 ms vs. I, red circles, τ = 9.4 ms), activation by 10 mM glutamate (black triangles, τ = 10 ms vs. green triangles, τ = 3.5 ms), and activation by 100 mM glutamate (black squares, τ = 13 ms vs. purple squares, τ = 8.5 ms). (E) Summary of the maximum change in fluorescence during fast fluorescence acquisition. The maximum normalized fluorescence change, $[\Delta F/F]_{Max}$, was calculated from the average peak intensity of the three final frames during the glutamate application in all three conditions: $[\Delta F/F]_{Max}$ (desensitized) = 0.025 ± 0.003, $[\Delta F/F]_{Max}$ (Active, 10 mM) = −0.021 ± 0.003, $[\Delta F/F]_{Max}$ (Active, 100 μM) = 0.009 ± 0.002. An unpaired two-tailed Student's t test gave P = 1.8E-09 (red vs. green circles), P = 8.9E-08 (red vs. purple circles), and P = 0.006 (green vs. purple circles). *P < 0.05; ***P < 0.0001. (F) Summary of ratios between signal amplitudes upon application of 10 mM and 100 μM glutamate (fluorescence intensity ratio = 0.49 ± 0.11, n = 6; current ratio = 0.36 ± 0.09, n = 6).
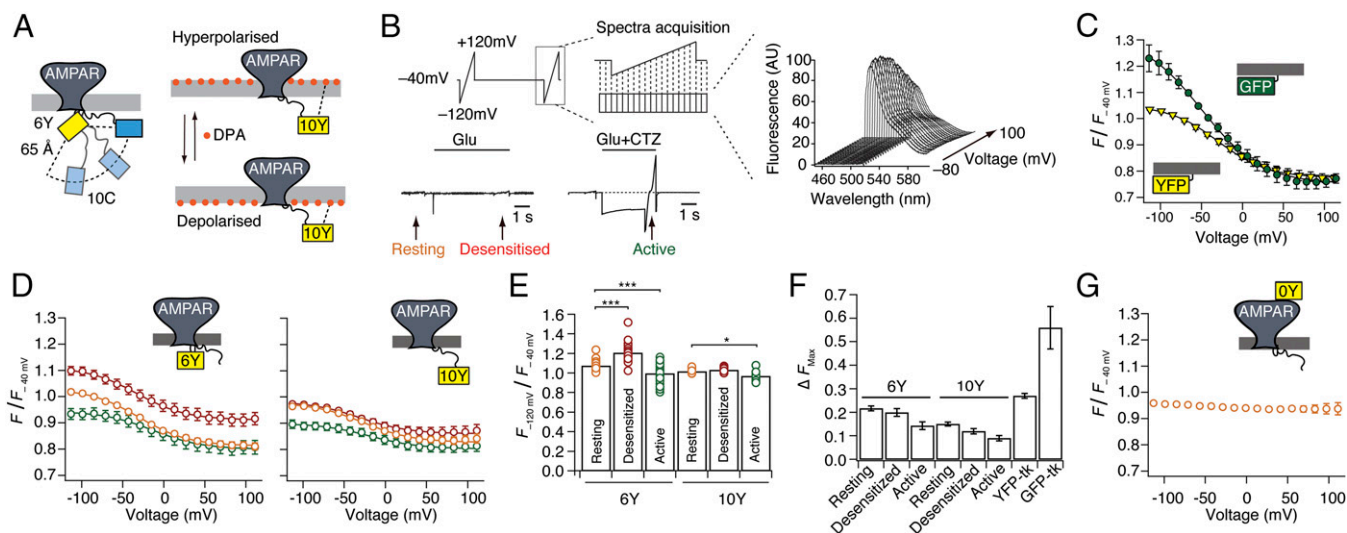
Fig. 5. Voltage-dependent quenching of intracellular fluorophores by DPA. (*A*) Cartoon showing 90° arc of possible positions of the 10C site relative to 6Y, given a separation of 65 Å (from FLIM measurements). The scheme shows DPA translocation through the plasma membrane with hyper- and depolarizing voltage, and the change in distance to the 10Y insertion. (*B*) Schematic representation of the voltage ramp protocol used to drive DPA translocation across the membrane and the corresponding spectra acquisition. This protocol was used to record voltage-dependent fluorescence quenching by DPA at distinct time points during long glutamate stimulation (5 s) of cells expressing YFP-tagged GluA2. For assessment of quenching in different receptor states, the ramps were timed to translate DPA across the membrane in resting (yellow), desensitized (red), and active states. Fifty-millisecond frames were collected during each ramp in the absence and presence of CTZ. The corresponding fluorescence emission spectra were normalized to fluorescence intensity at −40 mV. AU, arbitrary units. (*C*) Voltage-dependent quenching of membrane-bound GFP (green circles) and YFP (yellow triangles). To eliminate hysteresis effects, data points are the average of responses to negative- and positive-going ramps. Lines represent weighted sigmoid fits. (*D*) Quenching of fluorescence of GluA2-6Y (*Left*) and GluA2-10Y (*Right*) in resting (orange circles), desensitized (red circles), and active (green circles) states. (*E*) Summary of quenching at the hyperpolarizing limit, normalized to quenching at −40 mV for GluA2-6Y and GluA2-10Y. An unpaired two-tailed Student's *t* test gave *P* = 9.6E-9 for 6Y, desensitized vs. resting; *P* = 0.001 for 6Y, active vs. resting; and *P* = 0.008 for 10Y, active vs. resting. (*F*) Summary of extent of quenching for the I6 and I10 positions in the different functional states compared with membrane-bound YFP-tk and GFP-tk. The curve for the control position I0 was subtracted from all of the quenching curves before fitting to a sigmoid function. tk, truncated k-ras sequence (see *Materials and Methods*). (*G*) Lack of voltage dependence of GluA2-0Y.

position was generally less pronounced than at the I6 position for all three receptor states. However, the voltage-dependent quenching suggested that in the resting and desensitized states, the I10 insert was 32 Å and 37 Å from the membrane, respectively, approaching considerably closer when the channel is activated (to about 15 Å). This analysis suggested that the magnitude of ΔF was reduced by a substantial background signal (60–80%). This level of intracellular fluorescence is consistent with measurements of fluorescent or radioactively labeled GluA2, which suggests that at least half is immature and resident in the endoplasmic reticulum in HEK cells during overexpression (36, 37).

The distances obtained from the analysis of YFP/DPA voltage-dependent quenching experiments, together with the distances obtained from the dual-insertion FRET/FLIM experiments, were fed into a probabilistic model of the fluorophore positions to build a state-dependent map of the intracellular domains in axial and radial coordinates (*Materials and Methods* and Fig. S7). This interpretation assumes that the intracellular parts of the four subunits behave in an approximately fourfold symmetrical manner, and relies exclusively on measurements made within subunits or between single subunits and the membrane. Fig. 6 shows cartoon representations of the resulting distance maps in the resting, active, and desensitized states, and thus gives an outline of the state-dependent movements. These model maps predict that the C terminus is extended roughly parallel to the membrane. Compared with the resting state, the C terminus and the turret insertion move closer to the membrane when the receptor is active, and the turret moves away from the membrane during desensitization.

As expected from the spheroid geometry of the whole-cell preparation, we were unable to detect any state-dependent anisotropy of fluorescence emission. To assess possible effects of donor anisotropy, we performed an explicit 3D calculation of FRET, assuming a planar membrane, restraining the tilt angle

of the donor dipole relative to the membrane normal, and with Monte Carlo assignment of the dipole orientation for DPA and of the donor in the membrane-parallel plane (*Materials and Methods* and Fig. S8). Consistent with existing analytical treatments and simulations (38, 39), constrained geometry did not substantially change the predicted quenching curves. The major effect was an effective reduction of R_0, bringing the region of positive slope of ΔF into a position (∼5 Å from the membrane) that cannot be reached due to the size of the donor. Thus, both experiment and theory were consistent with little influence of donor anisotropy.

To control that the quenching was specific to the axial positions of the fluorophores at I6 and I10, we assessed the quenching of YFP inserted at I0 for the same experiment. Being extracellular, the polarity of the fluorescence change should be inverted with respect to voltage. Consistent with the obligatory distal position of this insertion, some 100 Å from the membrane,
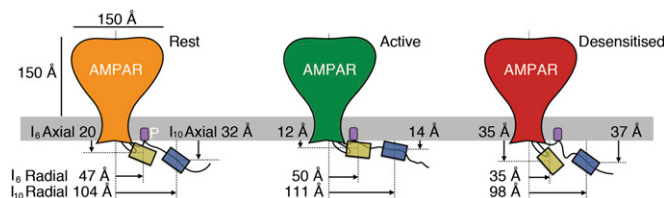

Fig. 6. Cartoon of intracellular movements during gating. A summary is provided of measured distances between the I6 (yellow) and I10 (blue) fluorophores in the resting (*Left*), active (*Middle*), and desensitized (*Right*) receptor states relative to the cell membrane (axial) and the channel center axis (radial). Note that the FRET distance can remain similar even if the fluorophores approach laterally, due to changes in axial separation.

Zachariassen et al.

we did not observe any dequenching with depolarization (Fig. 5G). This result confirms that the I6 and I10 quenching is specific to their axial positions, in close proximity to the membrane.

Discussion

The recent X-ray crystal structures of GluA2 and of the related NMDA-type iGluR GluN1/2B have provided rich information about the organization of the extracellular domains. However, in these structures, intracellular features are not resolved, and the structure of the CTD and the M1-M2 loop thus remains elusive (6), mandating the application of other methods to obtain structural information for these domains. In any case, methodologies that can provide information on protein conformational changes in the membrane of live cells are particularly valuable as complements to static structures. Resonance energy transfer methods (such as FRET and the luminescence-based variant, LRET) have proven potential to measure conformational changes in ion channels and receptors (18–22, 40, 41). In the present study, we address the structural configuration and conformational changes of the GluA2 CTD using FRET-enabled subunit constructs that contain dual incorporation of the FP-based FRET donor and acceptor fluorophores in the M1-M2 loop and the CTD to measure state-dependent positions of these two intracellular regions. The CTDs may assemble into a tertiary structure, contain some secondary structure elements, or simply act as flexible loops to allow scaffold proteins to bind directly to the polypeptide chain. The FRET efficiency of 13% from FLIM measurements on the GluA2-6Y-10C construct under resting conditions corresponds to an average donor/acceptor distance of ~65 Å, offering insight into the structural dimensions of the intracellular domains. Because the I10 insertions are not far from the membrane (Fig. S6), the fluorophores at the I6 insertions are likely positioned at a radius from the pore axis similar to the M4 helix. There are 39 amino acids between the end of M4 (Lys-848) and the I10 FP insert (after Asn-864 and including the 13-residue unstructured linker to the N terminus of the FP). Flexible polypeptides of 50 residues connecting FPs exhibit similar FRET distances (~60 Å) (42), which includes a minimum 20-Å separation due to volume exclusion from the size of the two fluorophores. Thus, although the C terminus might contain secondary structure elements, it must be largely disordered.

Patch-clamp fluorometry enabled us to correlate movements of the intracellular domains of GluA2 with receptor activity. Quenching by DPA revealed that both intracellular insertions move relative to the membrane during receptor activation. Perhaps most surprising of all was the ~15-Å movement of the C-terminal insertion site I10 toward the membrane during activation. The distal parts of the C-terminal tail are too far away to interact with the TMD. Therefore, this movement seems most likely to occur as the result of rearrangements in the TMD that interact with the membrane proximal regions of the CTD, encouraged perhaps by the palmitoyl anchor located here (43) and serving to change the effective length of this segment.

The state-dependent rearrangement of the intracellular region of GluA2 that we detect has several interesting implications. Although the ATD, LBD, and TMD exhibit high sequence homology across GluA1 to GluA4, and are structurally well-characterized (44), these regions are divergent and currently without structural information. Of particular interest is the functional role of the CTDs, which connect AMPARs with auxiliary proteins and some scaffolds involved in trafficking and synaptic anchoring (45). However, the CTD can also influence receptor function, for example, by being subject to phosphorylation, which apparently modulates important functional parameters such as channel conductance and open probability (46–49). Therefore, potential activity-dependent structural rearrangement of the CTD may be of importance for regulation of AMPAR function. Furthermore, it is interesting to note that recent work has shown that pushing synaptic AMPARs into different conformational states influences their mobility (50). Activity-dependent interaction with the membrane or other proteins through the CTD could alter lateral diffusion, consistent with observed effects related to receptor desensitization. Further studies of the conformational changes of the intracellular domains of AMPARs, for example, in relation to kinase and phosphatase activity as well as trafficking processes, will be needed to investigate this relationship.

The change in FRET at the intracellular domains that we observe in the presence of an extracellular ligand reveals mechanistic coupling between the extracellular LBD and the intracellular CTD that may have profound implications for the function of iGluRs. It suggests that binding of CTZ alters the conformational ensemble of resting receptors. Notably, although glutamate should not penetrate cells, CTZ, being highly lipophilic, may reach receptors in intracellular compartments. With this caveat in mind, CTZ does not open the channel, but its binding and stabilization of the LBD dimers may affect TMD conformation, which, in turn, propagates through to the intracellular domains. This communication must naturally be bidirectional, and parallel to the channel-gating reaction. The observed changes in fluorescence intensity during DPA quenching between the desensitized state and the closed resting state provide further evidence for multiple distinct closed states.

The slowness of some conformational changes (on the order of seconds) that we detected, being electrically silent and having no dependence on ion flux or channel block, may have little relevance for receptor gating during synaptic transmission. However, such conformations might be explored in other experiments that have long time scales, such as structural biology or biochemistry. Moreover, these measurements demonstrate that the AMPAR CTD can respond to processes much slower than neurotransmitter release, such as trafficking, biogenesis, and diffusional trapping of receptors. Notably, recent work using time-resolved measurement of FRET between FP-tagged CTDs in NMDA receptors (NMDARs) expressed in neurons found that CTD conformation is changed by agonist binding (51) and that CTD movements may be required for NMDAR-dependent synaptic plasticity (52). Together with our results, these findings warrant further studies aiming to understand how slow changes in conformation could correspond to the cell biology of iGluR function.

FRET has previously been applied to AMPARs to characterize the clamshell-closure motions within the LBDs (21, 53, 54) and the role of interfaces during desensitization (20). However, these studies relied on labeling of engineered cysteine residues, requiring removal of endogenous cysteines, either by mutation or truncation of the receptor (20, 41, 53, 55). In any case, labeling cysteines with organic dyes in mammalian cells (including neurons) is likely to be highly challenging. In contrast, inline FP insertions offer the opportunity to study a relatively uniform donor/acceptor-labeled receptor population without needing invasive, exogenous labels. The size of FP insertions is often cited as a drawback of the use of FPs as FRET pairs within proteins. However, screening of FP insertions in AMPAR subunits for function and fluorescence identified loops that allow benign insertion (23, 56, 57). These probes can report function, amplified by volume exclusion (the substantial size of the probe) and lever effects based on the probe displacement from the site of insertion (18). In agreement with previous work, we find that the four functional GluA2-CFP/YFP constructs, including the 6Y-10C FRET active construct, show largely unchanged kinetics and pharmacology compared with WT GluA2.

In summary, we have exploited inline insertion of FPs to study intrareceptor distances and conformational changes in AMPARs in live cells during fast gating. Given the conserved subunit architecture among iGluR subunits, the specific combinations of FP insertions that we have identified to be tolerated in GluA2 may potentially be useful for similar studies of other iGluRs.

Materials and Methods

Materials. Chemicals and reagents, including cDNA constructs, are described in detail in *SI Materials and Methods*.

Expression and Analysis of FP-Tagged GluA2 Constructs. Cell culture procedures and confocal microscopy analysis are described in *SI Materials and Methods*.

Oocyte Two-Electrode Voltage-Clamp Electrophysiology. Mature female *Xenopus laevis* oocytes prepared as previously described (47) and injected with 25 nL of cRNA encoding GluA2 constructs (1 ng/nL). Recordings were performed 3–6 d postinjection using a two-electrode voltage-clamp (OC-725C; Warner Instruments) under continuous perfusion with frog Ringer's solution [115 mM NaCl, 2 mM KCl, 1.8 mM BaCl$_2$, 5 mM Hepes (pH 7.6)] at room temperature at holding potentials of −40 to −80 mV. Concentration–response curves for inhibitors and positive modulators were constructed by measuring the current induced by a given concentration of glutamate, followed by application of increasing concentrations of test compounds in the continued presence of glutamate. Agonist concentration–response curves were generated by measuring steady-state currents evoked by increasing concentrations of agonist. Typically, composite concentration–response data were obtained from measurements at six to 12 individual oocytes and fitted to a sigmoidal dose–response function described by Eq. 1:

$$I = I_{min} + \frac{(I_{max} - I_{min})}{1 + ([ligand]/X)^{n_H}},$$ [1]

where I is the steady-state current at a given test compound concentration, I_{max} is the maximum response plateau, I_{min} is the minimum response plateau, [*ligand*] is the concentration of test compound, and n_H is the Hill slope. X is either the IC$_{50}$ (concentration of antagonist producing 50% of I_{max}) or EC$_{50}$ (concentration of agonist or positive modulator producing 50% of I_{max}).

HEK293 Patch-Clamp Electrophysiology. GluA2 WT and dual-tagged and single-tagged GluA2-YFP-CFP receptors were expressed in HEK293 cells by transient transfection using CaPO$_4$ coprecipitation. For outside-out patch-clamp recordings, external solution contained 150 mM NaCl, 0.1 mM MgCl$_2$, 0.1 mM CaCl$_2$, and 5 mM Hepes (pH 7.3). The pipette solution contained 115 mM NaCl, 10 mM NaF, 0.5 mM CaCl$_2$, 1 mM MgCl$_2$, 5 mM Na$_4$BAPTA, 5 mM Hepes, and 10 mM Na$_2$ATP (pH 7.3). Outside-out patches were voltage-clamped at −60 mV, and the currents were recorded using Axograph X (Axograph Scientific) via an Instrutech ITC-18 interface (HEKA). The rate of desensitization (k_{des}) was determined by fitting a single exponential function to the current decay during a long (100 ms) pulse of 10 mM glutamate. The rate of deactivation (k_{deact}) was determined by fitting a single exponential function to the decay following a brief (1 ms) pulse of 10 mM glutamate. Recovery from desensitization was measured using a two-pulse protocol with variable interpulse intervals. The k_{rec} was determined by fitting the recovery data with a Hodgkin–Huxley-type function with a slope of 2 (13).

FLIM. To determine the fluorescence lifetime of CFP in live cells, time-correlated single-photon counting (TCSPC) was carried out on transfected HEK293T cells 48–72 h posttransfection. Cells were grown in six-well, glass-bottomed culture plates. Before imaging, cells were washed once with 2 mL phosphate buffered saline with calcium and magnesium (PBSCM) per well and incubated with PBSCM. FLIM measurements were performed on a Leica SP2 laser-scanning confocal microscope equipped with a Hamamatsu R3809U-52 photomultiplier detector controlled by a Becker–Hickl TCSPC control module. Live cells were imaged in wells using a 63× 1.2-N.A. water HCX PL APO water-immersion objective with a 405-nm pulsed diode laser as an excitation source (PicoQuant). Cells were scanned for a period of 900 s with a laser power setting of 100%. The acquired FLIM images were analyzed using SPCImage software version 3.9.7 (Becker–Hickl) to determine the fluorescence lifetime (τ) for cell surface membrane-localized CFP in each pixel by fitting the fluorescence decay to a monoexponential function. This analysis yielded a distribution of lifetimes present that were fit with a single Gaussian function to yield the mean CFP lifetime and SD. For determination of FRET efficiency in GluA2-CFP/YFP receptors from measurements of donor lifetime, the τ_{CFP} needs to be obtained in the presence and absence of acceptor. For this purpose, a CFP/amber construct was created for each GluA2-

CFP/YFP construct. In these constructs, the ability of the YFP to serve as a FRET acceptor has been destroyed by a single point mutation (Y67C; amber) (26), and thus allows measurement of the CFP lifetime in the absence of FRET. From these values, FRET efficiency was calculated using Eq. 2:

$$E = 100\% \times \left(1 - \frac{\tau_{CFP-YFP}}{\tau_{CFP-amber}}\right),$$ [2]

where E is the FRET efficiency and $\tau_{CFP-YFP}$ and $\tau_{CFP-amber}$ are the lifetimes of CFP in the presence of YFP or the amber mutant of YFP, respectively.

Patch-Clamp Fluorometry. Whole HEK293 cells were lifted into the outflow of a piezo-driven fast solution switcher for activation by glutamate. For whole-cell patch-clamp recordings, the external solution contained 158 mM NaCl, 20 mM Hepes, 3 mM KCl, and 1 mM CaCl$_2$ (pH 7.4). The internal pipette solution contained 135 mM KCl, 20 mM KF, 20 mM Hepes, 3 mM NaCl, 1 mM MgCl$_2$, and 2 mM EGTA (pH 7.4). For quenching measurements, cells were perfused with DPA (5 μM) in both control and test barrels to avoid artifacts due to DPA washing in and out during solution exchange. Excitation by 445-nm and 514-nm laser lines (TOPTICA MLE) for CFP and YFP, respectively, was directed through a manual total internal reflection fluorescence (TIRF) input to an Olympus IX-81 microscope and focused to the back focal plane of a 20× Olympus objective. The emitted light was passed through the slit of a spectrograph (SP2156 Princeton Instruments) onto a grating (300/500 nm), and the resulting spectra were imaged by a ProEm 512 electron multiplying charge-coupled device (EMCCD) camera (Princeton Instruments). For ratiometric FRET recordings, filters specific to donor and acceptor wavelengths were alternated using the fluorescence turret under computer control (using a reverse-engineered serial connection to the IX-81 microscope, written in-house in Python). EMCCD acquisition rates were from 1 to 100 Hz, and the electron-multiplying gain was commonly set to 25. Ratiometric FRET calculations were performed as described (31). In DPA quenching experiments, we calculated the fractional fluorescence change ($\Delta F/F$) for the jth acquisition frame in a set of n frames relative to the intensity measured during the first frame in the presence of DPA (F_1) according to Eq. 3:

$$[\Delta F/F]_j = \frac{F_j - F_1}{F_1}, j = 1 \ldots n.$$ [3]

A background fluorescence signal was recorded in the absence of DPA and subtracted from each recording to correct for minor optical artifacts arising from the mechanical action of solution exchange. For control of DPA voltage dependence, HEK293 cells were transiently transfected with plasmids encoding GFP and YFP fused to a truncated k-ras membrane anchor sequence (KKKKKKSKTKCVIM) (58).

Calculations of Quenching and Distance Determination. Detailed descriptions for the calculations used for determination of FP quenching and distances are provided in *SI Materials and Methods*.

Data and Statistical Analysis. Data and statistical analyses were performed using GraphPad Prism 4.0 (GraphPad, Inc.) or IGOR Pro (Wavemetrics). Unless otherwise stated, values were compared by ANOVA.

1. Traynelis SF, et al. (2010) Glutamate receptor ion channels: Structure, regulation, and function. *Pharmacol Rev* 62(3):405–496.
2. Mayer ML (2011) Emerging models of glutamate receptor ion channel structure and function. *Structure* 19(10):1370–1380.
3. Rozov A, Jerecic J, Sakmann B, Burnashev N (2001) AMPA receptor channels with long-lasting desensitization in bipolar interneurons contribute to synaptic depression in a novel feedback circuit in layer 2/3 of rat neocortex. *J Neurosci* 21(20):8062–8071.
4. DiGregorio DA, Rothman JS, Nielsen TA, Silver RA (2007) Desensitization properties of AMPA receptors at the cerebellar mossy fiber granule cell synapse. *J Neurosci* 27(31):8344–8357.
5. Yelshanskaya MV, Li M, Sobolevsky AI (2014) Structure of an agonist-bound ionotropic glutamate receptor. *Science* 345(6200):1070–1074.
6. Sobolevsky AI, Rosconi MP, Gouaux E (2009) X-ray structure, symmetry and mechanism of an AMPA-subtype glutamate receptor. *Nature* 462(7274):745–756.
7. Chen L, Dürr KL, Gouaux E (2014) X-ray structures of AMPA receptor-cone snail toxin complexes illuminate activation mechanism. *Science* 345(6200):1021–1026.
8. Dürr KL, et al. (2014) Structure and dynamics of AMPA receptor GluA2 in resting, pre-open, and desensitized states. *Cell* 158(4):778–792.
9. Meyerson JR, et al. (2014) Structural mechanism of glutamate receptor activation and desensitization. *Nature* 514(7522):328–334.
10. Horning MS, Mayer ML (2004) Regulation of AMPA receptor gating by ligand binding core dimers. *Neuron* 41(3):379–388.
11. Sun Y, et al. (2002) Mechanism of glutamate receptor desensitization. *Nature* 417(6886):245–253.

12. Hogner A, et al. (2003) Competitive antagonism of AMPA receptors by ligands of different classes: Crystal structure of ATPO bound to the GluR2 ligand-binding core, in comparison with DNQX. *J Med Chem* 46(2):214–221.

13. Plested AJ, Mayer ML (2009) AMPA receptor ligand binding domain mobility revealed by functional cross linking. *J Neurosci* 29(38):11912–11923.

14. Armstrong N, Gouaux E (2000) Mechanisms for activation and antagonism of an AMPA-sensitive glutamate receptor: Crystal structures of the GluR2 ligand binding core. *Neuron* 28(1):165–181.

15. Armstrong N, Jasti J, Beich-Frandsen M, Gouaux E (2006) Measurement of conformational changes accompanying desensitization in an ionotropic glutamate receptor. *Cell* 127(1):85–97.

16. Lu W, Roche KW (2012) Posttranslational regulation of AMPA receptor trafficking and function. *Curr Opin Neurobiol* 22(3):470–479.

17. Huganir RL, Nicoll RA (2013) AMPARs and synaptic plasticity: The last 25 years. *Neuron* 80(3):704–717.

18. Miranda P, et al. (2013) State-dependent FRET reports calcium- and voltage-dependent gating-ring motions in BK channels. *Proc Natl Acad Sci USA* 110(13):5217–5222.

19. Zheng J, Zagotta WN (2000) Gating rearrangements in cyclic nucleotide-gated channels revealed by patch-clamp fluorometry. *Neuron* 28(2):369–374.

20. Gonzalez J, Du M, Parameshwaran K, Suppiramaniam V, Jayaraman V (2010) Role of dimer interface in activation and desensitization in AMPA receptors. *Proc Natl Acad Sci USA* 107(21):9891–9896.

21. Gonzalez J, Rambhadran A, Du M, Jayaraman V (2008) LRET investigations of conformational changes in the ligand binding domain of a functional AMPA receptor. *Biochemistry* 47(38):10027–10032.

22. Du M, Rambhadran A, Jayaraman V (2008) Luminescence resonance energy transfer investigation of conformational changes in the ligand binding domain of a kainate receptor. *J Biol Chem* 283(40):27074–27078.

23. Sheridan DL, Robert A, Cho CH, Howe JR, Hughes TE (2006) Regions of alpha-amino-5-methyl-3-hydroxy-4-isoxazole propionic acid receptor subunits that are permissive for the insertion of green fluorescent protein. *Neuroscience* 141(2):837–849.

24. Doherty AJ, Collingridge GL, Henley JM (1997) GFP fusion proteins and AMPA receptor trafficking. *Biochem Soc Trans* 25(3):540S.

25. Markwardt ML, et al. (2011) An improved cerulean fluorescent protein with enhanced brightness and reduced reversible photoswitching. *PLoS One* 6(3):e17896.

26. Koushik SV, Chen H, Thaler C, Puhl HL, 3rd, Vogel SS (2006) Cerulean, Venus, and VenusY67C FRET reference standards. *Biophys J* 91(12):L99–L101.

27. Shimozono S, et al. (2006) Concatenation of cyan and yellow fluorescent proteins for efficient resonance energy transfer. *Biochemistry* 45(20):6267–6271.

28. Karasawa S, Araki T, Nagai T, Mizuno H, Miyawaki A (2004) Cyan-emitting and orange-emitting fluorescent proteins as a donor/acceptor pair for fluorescence resonance energy transfer. *Biochem J* 381(Pt 1):307–312.

29. Clements JD, Lester RA, Tong G, Jahr CE, Westbrook GL (1992) The time course of glutamate in the synaptic cleft. *Science* 258(5087):1498–1501.

30. Partin KM, Fleck MW, Mayer ML (1996) AMPA receptor flip/flop mutants affecting deactivation, desensitization, and modulation by cyclothiazide, aniracetam, and thiocyanate. *J Neurosci* 16(21):6634–6647.

31. Zheng J, Zagotta WN (2003) Patch-clamp fluorometry recording of conformational rearrangements of ion channels. *Sci STKE* 2003(176):PL7.

32. Benz R, Läuger P (1977) Transport kinetics of dipicrylamine through lipid bilayer membranes. Effects of membrane structure. *Biochim Biophys Acta* 468(2):245–258.

33. Chanda B, et al. (2005) A hybrid approach to measuring electrical activity in genetically specified neurons. *Nat Neurosci* 8(11):1619–1626.

34. Wang Y, et al. (2010) The calcium store sensor, STIM1, reciprocally controls Orai and CaV1.2 channels. *Science* 330(6000):105–109.

35. Fernández JM, Taylor RE, Bezanilla F (1983) Induced capacitance in the squid giant axon. Lipophilic ion displacement currents. *J Gen Physiol* 82(3):331–346.

36. Penn AC, Williams SR, Greger IH (2008) Gating motions underlie AMPA receptor secretion from the endoplasmic reticulum. *EMBO J* 27(22):3056–3068.

37. Shanks NF, Maruo T, Farina AN, Ellisman MH, Nakagawa T (2010) Contribution of the global subunit structure and stargazin on the maturation of AMPA receptors. *J Neurosci* 30(7):2728–2740.

38. Loura LM (2012) Simple estimation of Förster Resonance Energy Transfer (FRET) orientation factor distribution in membranes. *Int J Mol Sci* 13(11):15252–15270.

39. van der Meer BW (2002) Kappa-squared: From nuisance to new sense. *J Biotechnol* 82(3):181–196.

40. Cha A, Bezanilla F (1997) Characterizing voltage-dependent conformational changes in the Shaker K+ channel with fluorescence. *Neuron* 19(5):1127–1140.

41. Rambhadran A, Gonzalez J, Jayaraman V (2011) Conformational changes at the agonist binding domain of the N-methyl-D-aspartic acid receptor. *J Biol Chem* 286(19):16953–16957.

42. Ohashi T, Galiacy SD, Briscoe G, Erickson HP (2007) An experimental study of GFP-based FRET, with application to intrinsically unstructured proteins. *Protein Sci* 16(7):1429–1438.

43. Hayashi T, Rumbaugh G, Huganir RL (2005) Differential regulation of AMPA receptor subunit trafficking by palmitoylation of two distinct sites. *Neuron* 47(5):709–723.

44. Baranovic J, Plested AJ (2016) How to build the fastest receptor on earth. *Biol Chem* 397(3):195–205.

45. Malinow R, Malenka RC (2002) AMPA receptor trafficking and synaptic plasticity. *Annu Rev Neurosci* 25:103–126.

46. Derkach V, Barria A, Soderling TR (1999) Ca2+/calmodulin-kinase II enhances channel conductance of alpha-amino-3-hydroxy-5-methyl-4-isoxazolepropionate type glutamate receptors. *Proc Natl Acad Sci USA* 96(6):3269–3274.

47. Kristensen AS, et al. (2011) Mechanism of Ca2+/calmodulin-dependent kinase II regulation of AMPA receptor gating. *Nat Neurosci* 14(6):727–735.

48. Banke TG, et al. (2000) Control of GluR1 AMPA receptor function by cAMP-dependent protein kinase. *J Neurosci* 20(1):89–102.

49. Jenkins MA, et al. (2014) Regulation of GluA1 α-amino-3-hydroxy-5-methyl-4-isoxazolepropionic acid receptor function by protein kinase C at serine-818 and threonine-840. *Mol Pharmacol* 85(4):618–629.

50. Constals A, et al. (2015) Glutamate-induced AMPA receptor desensitization increases their mobility and modulates short-term plasticity through unbinding from Stargazin. *Neuron* 85(4):787–803.

51. Dore K, Aow J, Malinow R (2015) Agonist binding to the NMDA receptor drives movement of its cytoplasmic domain without ion flow. *Proc Natl Acad Sci USA* 112(47):14705–14710.

52. Aow J, Dore K, Malinow R (2015) Conformational signaling required for synaptic plasticity by the NMDA receptor complex. *Proc Natl Acad Sci USA* 112(47):14711–14716.

53. Du M, Reid SA, Jayaraman V (2005) Conformational changes in the ligand-binding domain of a functional ionotropic glutamate receptor. *J Biol Chem* 280(10):8633–8636.

54. Ramaswamy S, et al. (2012) Role of conformational dynamics in α-amino-3-hydroxy-5-methylisoxazole-4-propionic acid (AMPA) receptor partial agonism. *J Biol Chem* 287(52):43557–43564.

55. Rambhadran A, Gonzalez J, Jayaraman V (2010) Subunit arrangement in N-methyl-D-aspartate (NMDA) receptors. *J Biol Chem* 285(20):15296–15301.

56. Sheridan DL, et al. (2002) A new way to rapidly create functional, fluorescent fusion proteins: Random insertion of GFP with an in vitro transposition reaction. *BMC Neurosci* 3:7.

57. Midgett CR, Gill A, Madden DR (2012) Domain architecture of a calcium-permeable AMPA receptor in a ligand-free conformation. *Front Mol Neurosci* 4:56.

58. Wang D, Zhang Z, Chanda B, Jackson MB (2010) Improved probes for hybrid voltage sensor imaging. *Biophys J* 99(7):2355–2365.

59. Nagai T, et al. (2002) A variant of yellow fluorescent protein with fast and efficient maturation for cell-biological applications. *Nat Biotechnol* 20(1):87–90.

60. Miller WG, Goebel CV (1968) Dimensions of protein random coils. *Biochemistry* 7(11):3925–3935.